Effect of Graphene Nanoplatelets Structure on the Properties of Acrylonitrile–Butadiene–Styrene Composites

S. Dul,[1] **L. Fambri**,[1] **C. Merlini**,[2] **G.M.O. Barra**,[2] **M. Bersani**,[3] **L. Vanzetti**,[3] **A. Pegoretti**[1]
[1] *Department of Industrial Engineering and INSTM Research Unit, University of Trento, Trento, Italy*

[2] *Department of Mechanical Engineering, Federal University of Santa Catarina, Florianópolis, Santa Catarina, Brazil*

[3] *Centre for Materials and Microsystems, Fondazione Bruno Kessler, Trento, Italy*

In this study, the effects of various types of commercial graphene nanoplatelets (XG Sciences xGnP M5, C300, C500, and C750) on the thermal, electromagnetic shielding (EMI SE), electrical and mechanical behavior of an acrylonitrile–butadiene–styrene (ABS) copolymer matrix were investigated. The selected nanofillers were characterized and compared in term of surface area, different oxygen content, dimension and density (X-ray photoelectron spectroscopy, scanning electron microscopy, and helium pycnometry). Graphene nanoplatelets were dispersed in ABS by direct melt compounding at 2, 4, and 8 wt%. Melt flow index (MFI) values almost linearly decreased with all the type of xGnPs, especially with the highest surface area nanofiller (C750). Moreover, EMI SE of neat ABS was improved from −0.7 dB to −2.5 dB (increase more than 3 times) for xGnP (C300, C500, and C750) and to −6.2 dB (increase about 9 times) for xGnP-M5, in agreement with proportional reduction of electrical resistivity. xGnP-M5 also resulted in being most effective in enhancing the tensile modulus which improved up to 64%, while a maximum increment of about 20% was obtained with the others xGnP nanoparticles. However, yield stress slightly decreased for xGnP-M5 (about −9%) and remained fairly constant for others nanofillers. Halpin–Tsai model used to predict the tensile modulus of the nanocomposites suggested that graphene nanoplatelets were randomly oriented in the ABS matrix in a three-dimensional (3D) manner. POLYM. COMPOS., 40: E285–E300, 2019. © 2017 Society of Plastics Engineers

INTRODUCTION

Among engineering thermoplastic acrylonitrile–butadiene–styrene (ABS) copolymer is extensively used due to its good properties such as high rigidity and strength, easy processing characteristics, chemical resistance, dimensional stability, and good surface finishing. This thermoplastic polymer has been used for various applications in the automotive sector, electronic devices, domestic appliances, etc. [1–5]. Recently, ABS has also been used massively in fused deposition modeling application [6–9].

Due to its outstanding mechanical and transport properties [10–12], in recent year graphene has attracted the attention of several researchers as a nanofiller for multifunctional composites. In fact, graphene-based nanocomposites are massively investigated [11, 13–23]. In particular, some studies on ABS with graphite/graphene as novel fillers were also reported. Pandey et al. [24] also investigated graphite flake-reinforced ABS up to high loading content (40 vol%). At mentioned loading level of filler, flexural modulus and loss modulus were enhanced by 92% and 250%, respectively. However, the tensile strength and elongation at break were reduced. They also reported an improvement of thermal conductivity of about 250%. Heo et al. [25] prepared and characterized octadecylamine–graphene (C18-graphene) incorporated in ABS. Homogeneous dispersion of the hybrid graphene filler, resulting in the improvement of thermal and tensile properties. Sachdev et al. [26] prepared graphite/ABS samples through compression molding and reported their electromagnetic interference shielding and conductivity properties. At 15 wt% of graphene, electromagnetic shielding (EMI SE), and conductivity values of −60 dB and 0.166 S/cm were respectively achieved. Ben Difallah et al. [4] reported ABS polymer matrix filled with graphite powder through melt blending. Graphite powder decreased the mechanical properties of neat ABS but improved the friction and wear resistance especially at a filler loading of 7.5 wt%. Gao et al. [27] reported on

---

Correspondence to: A. Pegoretti; e-mail: alessandro.pegoretti@unitn.it
DOI 10.1002/pc.24645

TABLE 1. Characteristics of as-received graphene nanoplatelets (xGnP). Geometrical size according to manufacturer, atomic percentage of surface elemental composition and density, as measured by XPS analysis and helium pycnometry, respectively.

Samples	Lateral dimension[a] (μm)	Thickness[a] (nm)	C (%)	O (%)[b]	N (%)	S (%)	Density (g/cm^3)
xGnP-M5	~5	6	95.1	2.0 + 2.2	0.3	0.4	2.06 ± 0.03
xGnP-C300	1–2	<2	96.0	3.8 + 0.0	0.2	—	2.33 ± 0.02
xGnP-C500	1–2	<2	93.8	5.9 + 0.0	0.3	—	2.30 ± 0.02
xGnP-C750	1–2	<2	92.9	6.7 + 0.0	0.4	—	2.21 ± 0.03

[a] From producer data sheets [32].

[b] Contribute of ether or alcohol groups and carbonyl groups (see Fig. 2b and text).

ABS filled with graphene nanosheet with a low electrical percolation threshold of 0.13 vol% due to the adopted coagulation method. Uhl et al. [28] investigated ABS filled with virgin graphite and expanded graphite. However, the mechanical properties were not enhanced. Hong et al. [29] reported on ABS/graphene nanocomposites combined with metal hydroxide nanorods with enhanced mechanical and flame retardant properties. Dahiya et al. [30] found that graphite dispersed in ABS can improve the electrical and dielectric properties at a loading level of 7.6 vol%. Pour et al. [31] studied polycarbonate/ABS polymer blend reinforced with graphene nanoplatelets. One size of graphene nanoplatelets (GNP) with a length of 15 μm was used leading to improvements of 30 and 54% of tensile and flexural modulus at a content of 3 wt%.

The objective of this study is to investigate the comparative influence of four commercially available graphene nanoplatelets (M5, C300, C500, and C750) with different size and surface area (120–700 m^2/g) on the properties and processability of melt compounded ABS nanocomposites. In particular, melt flow index (MFI), thermal transitions, electromagnetic shielding efficiency (EMI SE), and tensile mechanical properties were investigated as a function of filler type and content. The Halpin–Tsai model was successfully used to fit the experimental values of tensile modulus. To the best of authors' knowledge, material properties and modeling of xGnP M5, C300, C500, C750 in ABS matrix have never been previously reported in the open scientific literature.

EXPERIMENTAL

Materials

Four grades of graphene nanoplatelets (xGnP), namely M5, C300, C500, and C750 with increasing surface area, i.e. $120-150$ m^2/g, 300 m^2/g, 500 m^2/g, and 750 m^2/g, respectively [32], were purchased from XG Sciences, Lansing, MI. Informations available from the producer on the lateral dimensions and the thickness of the nanoplatelets are reported in Table 1.

Acrylonitrile–butadiene–styrene (ABS) polymer (tradename Sinkral®L322) was provided by Versalis S.p.A. (Mantova, Italy). According to producer's technical data sheet, the polymer has a density of 1.04 g/cm^3 and a MFI of 26 cm^3/10 min at 220°C/10 kg [33]. According to technical suggestions, ABS chips were dried under vacuum at least 2 h at 80°C before processing.

Materials Processing and Sample Preparations

xGnP at concentration of 2, 4, and 8 wt% was mixed with neat ABS by melt compounding in a co-rotating Thermo-Haake Polylab Rheomix internal mixer (temperature of 190°C; rotor speed of 90 rpm for 15 min). Batches of about 50 g were produced for each composition. The compounded materials were hot pressed at 190°C in a Carver Laboratory press for 10 min under a pressure of 3.9 MPa, to obtain square plates (160 × 160 mm) with thickness in the range from 1.2 to 2 mm. Neat ABS was also processed under the same conditions. Dog-bone samples for tensile test were prepared by a Ceast manual punching machine. The remaining parts of the plates were used for further characterization (scanning electron microscopy, melt index, thermogravimetric analysis, and differential scanning calorimetry).

Material Testing and Characterization Techniques

Scanning Electron Microscopy (SEM). Morphology of xGnP particles and fracture surface of nanocomposites were studied by using a Carl Zeiss AG Supra 40 field emission scanning electron microscope (FESEM).

Graphene nanoplatelets were dispersed in chloroform with a concentration of 0.1 mg/ml and sonicated for 10 min by Ultrasonic Processor UP400S. Finally, graphene dispersion solution was directly dropped and evaporated onto aluminum plates for observation at an acceleration voltage of 10 kV. Nanocomposites were fractured in liquid nitrogen, and the fracture surfaces were observed at an acceleration voltage of 3 kV. Representative micrographs at different level of magnification were selected.

X-Ray Photoelectron Spectroscopy (XPS). To identify the surface chemical compositions of xGnPs, X-ray photoelectron spectroscopy (XPS) was performed using a Kratos Axis Ultra DLD instrument (Kratos Analytical, Manchester, UK) equipped with a hemispherical analyzer and a monochromatic AlKα (1,486.6 eV) X-ray source, in spectroscopy mode at two levels of resolution (survey and core). The emission angle between the axis of the analyzer and the normal to the surface of samples was 0°. First, a survey (for binding energy up to 1,300 eV) was collected for each sample to identify the elements on the sample surface. Afterwards at higher energy resolution, the core levels C 1s, O 1s, N 1s, and S 2s were also collected to evaluate the chemical differences between the samples. The quantification, reported as relative element percentage, for each sample was performed using the integrated area of the fitted lines, after Shirley background subtraction, and correcting for the atomic sensitivity factors.

Density Measurement. Density measurements of graphene nanoplatelets were carried out by helium pycnometry technique on a Micromeritics® Accupyc 1330 helium pycnometer (Norcross), performing 99 measurements on about 0.8 g and 1.7 g of C and M powder, respectively, in a testing chamber of 10 cm^3 at a temperature of 23.0°C. High precision tungsten carbide balls were used for calibration.

MFI Test. The MFI measurements were carried out according to ASTM D 1238 standard (procedure A), through a Kayeness Co. model 4003DE capillary rheometer, at a temperature of 220°C with an applied load of 10 kg on samples with a mass of about 5 g (pre-heat and compaction time of about 5 min). The results represent the average of at least five measurements (standard deviation is reported).

Thermogravimetric Analysis (TGA). Thermal degradation was investigated through a Q5000 IR thermogravimetric analyzer (TA Instruments-Waters LLC, New Castle). The samples having a mass of about 10 mg were tested from 30°C to 800°C at a rate of 10°C/min under nitrogen flow of 15 ml/min. The maximum degradation temperatures ($T_{d,max}$) corresponds to the maximum of the first derivative of weight loss. The instrument was calibrated according producer standard; the balance sensitivity was 0.1 mg.

Differential Scanning Calorimetry. Differential scanning calorimetry (DSC) analysis was carried out by a Mettler DSC 30 calorimeter on samples of about 10 mg with a heating–cooling–heating cycle in the range between 30°C and 260°C at a rate of ±10°C/min flushing nitrogen at 100 ml/min. Glass transition temperature (T_g) of SAN phase was measured at the inflection point of the thermogram. Indium standard (melting point 156.6°C and melting enthalpy 28.5 J/g) was used for instrument calibration.

Electromagnetic Interference Shielding Effectiveness (EMI SE). The electromagnetic interference properties of ABS and nanocomposites were measured using an Agilent Technology PNA series network analyzer (N5230C Agilent PNA-L, Santa Clara, CA) and a standard rectangular waveguide in the X-band frequency range (8.2–12.4 GHz). The analysis was performed on samples with a width of 10 mm, length of 23 mm and thickness of 2 mm, and the S-parameters (S_{11}, S_{22}, S_{12}, S_{21}) were recorded over the X-band frequency range. At least three specimens were tested for each sample and the standard deviations were calculated.

Electrical Resistivity. The volume resistivity was measured according to the ASTM D257 by using a Keithley 6517A electrometer/High Resistance Meter and an 8009 Resistivity Test Fixture. Square specimens of 64 × 64 mm were tested at a constant voltage of 100 V. The values represent the average of three measurements.

Quasi-Static Tensile Test. Uniaxial tensile tests were carried out at room temperature through an Instron® 5969 machine equipped with a 50 kN load cell on ISO 527 type 1BA specimens with a gauge length of 30 mm and a thickness of 1.2 mm. Tests for elastic modulus determination were performed at a crosshead speed of 1 mm/min and the strain was monitored with an electrical extensometer Instron® Model 2620-601 (gage length of 12.5 mm). According to ISO 527 standard, the elastic modulus was determined as a secant value between strain levels of 0.05% and 0.25%. Yield stress (σ_y), strain at break (ε_b), and stress at break (σ_b) were evaluated at a crosshead speed of 10 mm/min without extensometer. At least five specimens were tested for each sample whose average value and standard deviation were evaluated.

RESULTS AND DISCUSSION

Characterization of xGnP

Figure 1 shows SEM images of different types of graphene nanoplatelets. It can be clearly observed that M5 nanoparticles show the largest size followed by C300, C500, and C750, respectively, in agreement with the corresponding surface area values. Graphene nanoparticle C300 and C500 resulted to be similar in size as illustrated in Figure 1b and 1c, whereas graphene C750 appeared as particulate nanofiller, rather than platelets structure, exhibiting a low aspect ratio in agreement with the observations of other authors [10, 21].

Figure 2a shows the XPS survey spectra of the four different xGnPs nanoparticles. As summarized in Table 1, carbon and oxygen are the main elements detected on the surface from the peaks at 285 and ~533 eV, with a very small amount of nitrogen (0.2–0.4%), as evidenced from the peak at about 400 eV for all nanofillers.

Details of the oxygen core level are shown in Figure 2b. Samples C750, C500, and C300 exhibit a similar O 1s peak, centered at about 533 eV, that can be attributed to oxydrilic and/or ether groups [34]; it is worthwhile to note that peak height increased with the surface area, reaching

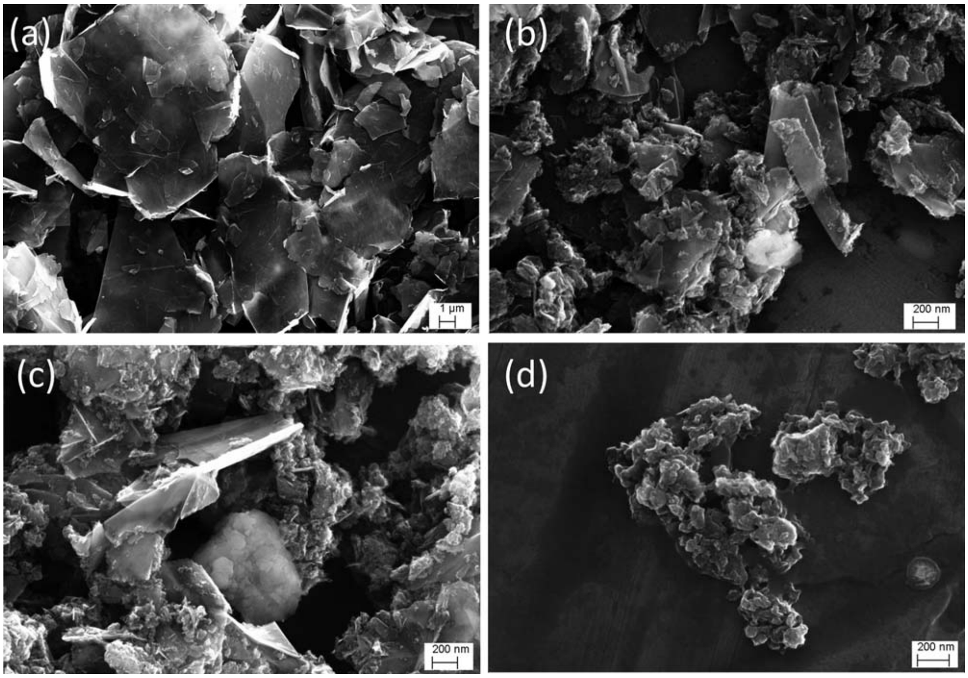

FIG. 1. SEM images of different type of graphene nanoplatelets: (a) M5, (b) C300, (c) C500, and (d) C750 after 10 min of sonication in chloroform.

the highest oxygen content of 6.7% for xGnP-750, due to smallest particle size resulting in a large proportion of edges, showing an analogous direct relationship with the surface area, as observed for sample C500 and C300.

However, M5 sample showed a total oxygen content of 4.2%, which is comparable to literature data [10], but it is higher than expected with respect to the surface area and the particle dimensions, that are definitively higher than C samples. The explanation could be found by the qualitative difference of O 1s signal observed for sample M5 (double peak) with a significant contribute of the peak at about 531 eV (see deconvolution in Figure 2b), that according literature is attributable to the carbonyl group [34]. Following partial integration, the quantitative analysis resulted in an almost equivalent contribute of the carbonyl and the ether/alcohol components, being 2.2% of $>C{=}O$ and 2.0% of $-O-$ and $-OH$ groups. Taking into consideration this latter value, the ether/alcohol content of graphene particles appeared almost directly proportional to the surface area.

The peculiar aspect of M5 graphene is furtherly evidenced from the surface chemical composition with few traces of sulfur, as documented in Figure 2a, by the S 2s and S 2p peaks at 225 and about 165 eV, respectively.

A comparative enlargement of the S 2p zone (Fig. 2c) confirmed the absence of sulfur in the three graphenes of Series C, whereas sample M5 evidenced two type of sulfur, in particular the peaks at 163.8 eV and 168.1 eV are respectively assigned to $2p_{2/3}$ and to oxidized sulfur groups according to Quan et al. [35].

The density data of graphene nanoplatelets are reported in Table 1. The density of C300 is slightly higher than that of C500 and higher than that of C750, evidencing an almost inverse dependence of their density on the content of ether/alcohol groups and on the surface area. However, M5 shows lower density (2.06 g/cm^3) with respect to the grade C nanoparticles (2.21–2.33 g/cm^3), in conformity to the qualitatively and quantitatively different chemical composition of the surface of grade M graphene, due to the presence of carbonyl and sulfur containing groups, as revealed by XPS.

Melt Flow Index

Melt compounding and hot pressing processes lead to an increase in the MFI of neat ABS from 25.4 ± 1.4 g/10 min to 34.8 ± 1.4 g/10 min. This lower viscosity can be attributed to the chain scission occurred during the process, after the consumption of antioxidant stabilizers. As reported by Boldizar and Möller [36], melt volume rate of neat ABS significantly increased (up to about two times) after a repetition of seven consecutive extrusion processes and accelerated aging. The effect of the various types of xGnP nanoparticles on MFI of ABS nanocomposites is compared in Figure 3. The almost linear decrease in MFI with the percentage of nanofillers suggests that a good dispersion of graphene has been reached with formation of a nanofiller network, determining a significant constrain of the polymer flow, and consequently an increase in viscosity, in agreement with literature on graphene-based nanocomposites [37–41]. At the highest concentration of graphene (8 wt%), MFI was reduced by about 50% for M5, whereas higher reduction was observed for grade C nanoparticles, i.e. about 53%, 56%, and 67% for nanofillers with specific

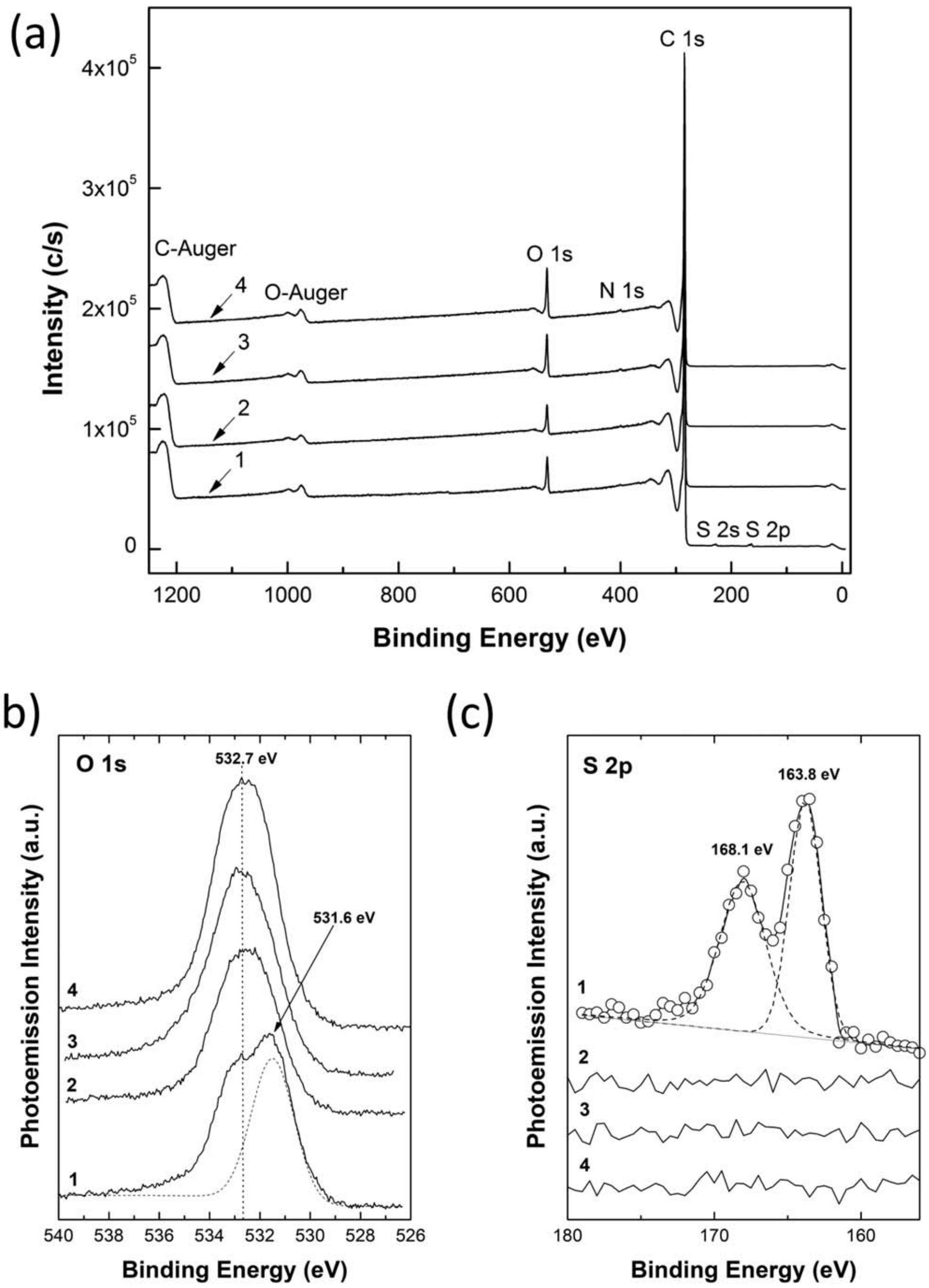

FIG. 2. XPS spectra of xGnP-M5 (1), C300 (2), C500 (3), and C750 (4): (a) XPS survey; (b) oxygen core level (O 1s); (c) sulfur core level (S 2p).

surface area of 300, 500, and 750 g/m^2, respectively. The higher the nanofiller surface area, the higher the rate of reduction of MFI and the higher the viscosity. In prior work, the larger specific surface area of fillers was also reported to increase the viscosity of an unsaturated polyester resin, due to increasing of the interaction between the matrix and the particles [42].

Thermal Stability

The thermal stability of graphene–ABS composites has been widely reported in the scientific literature [24, 25, 29, 43]. In Figure 4, the thermograms of neat ABS and its nanocomposites at the highest content of graphene are plotted. Neat ABS and ABS–graphene composites decompose in one single step of degradation in inert (nitrogen) atmosphere regardless the effect of graphene. This behavior is probably attributed to the butadiene particle content in ABS structure [44]. In addition, relative chart residue of ABS composite in Figure 4b linearly increases with the amount of nanofiller up to 7.6–10%. As reported in Table 2, the maximum degradation temperature ($T_{\mathrm{d,max}}$) seems not to be affected by graphene content. In addition, $T_{\mathrm{d,max}}$ slightly increases for M5 composites but drop for

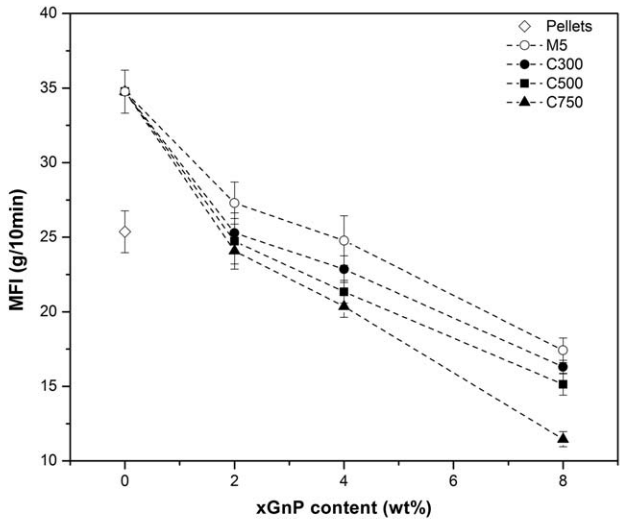

FIG. 3. MFI of ABS nanocomposites as function of xGnPs.

C500 and C750. This behavior could be induced by the different size of graphene flakes, as documented in Figure 1. In general, larger flakes can hinder the diffusion of volatiles products generated by polymer decomposition. In particular, as the concentration of graphene in ABS increases, the maximum mass loss rate (MMLR) is progressively reduced. This behavior was also observed in ABS–carbon nanotube [44] and polypropylene–graphene composites [45]. The high surface area of graphene (e.g., C500 and C750) reduces the value of MMLR which is expected as a result of stronger interphase bonding between the matrix and the C-type graphene.

Differential Scanning Calorimetry

Typical DSC thermograms of ABS and relative nanocomposites are illustrated in Figure 5. Two transitions can be clearly observed in both first and second heating scan of DSC analysis. At about 101°C ABS displays a glass transition signal of the amorphous styrene–acrylonitrile copolymer (SAN) phase [5, 43, 46], followed by another signal at about 137°C. Differently from the interpretation given by Singh and Ghosh [47], this endothermic peak is associated to the melting peak of a mold lubricant. According to scientific literature, this mold lubricant could contain fatty acid amide (FAA) [48] or polyamide [49], as previously discussed in details [50].

Table 3 summarizes the main thermal parameters of ABS pellets and compression molded plates. In particular T_g of SAN phase, melting temperature (T_m) and melting heat (ΔH_m) of mold lubricant for all the compositions are shown. The mold lubricant content in ABS could be evaluated as 3.6% by wt, according to the ratio of the melting heat of pellets and the reference enthalpy 98.8 J/g of pure lubricant [51].

In both first and second heating scans, the presence of M5 nanoparticles does not significantly affect the T_g of ABS matrix, whereas a slight increase in T_g was observed with other xGnP (up to about 2°C in the case of 8% of C750). Moreover, the melting temperature of the mold lubricant (T_m) decreased after addition of graphene (by 7°C for C750 filled samples). The higher the graphene content and/or the higher the surface area of the filler, the lower the melting temperature. Similarly, a significant decrease in melting heat was found in ABS composites, with values lower than that expected from composition, suggesting an interaction between mold lubricant and graphene. This fact is more evident in the second DSC heating, after a controlled cooling scan at −10°C/min, where all the samples exhibited not only an increase in T_g and T_m, but also a decrease in the melting heat. This latter effect is well evidenced by considering the normalized melting heat of mold lubricant, ΔH_N, referred to the fraction of ABS matrix, according to the equation:

$$\Delta H_N = \frac{\Delta H_m}{1 - w_f} \tag{1}$$

where w_f is filler fraction in nanocomposites. Figure 6 shows the reduction of the melting heat of lubricant (ΔH_N) in the second DSC scan with the increase in the surface area and/or of the content of xGnP.

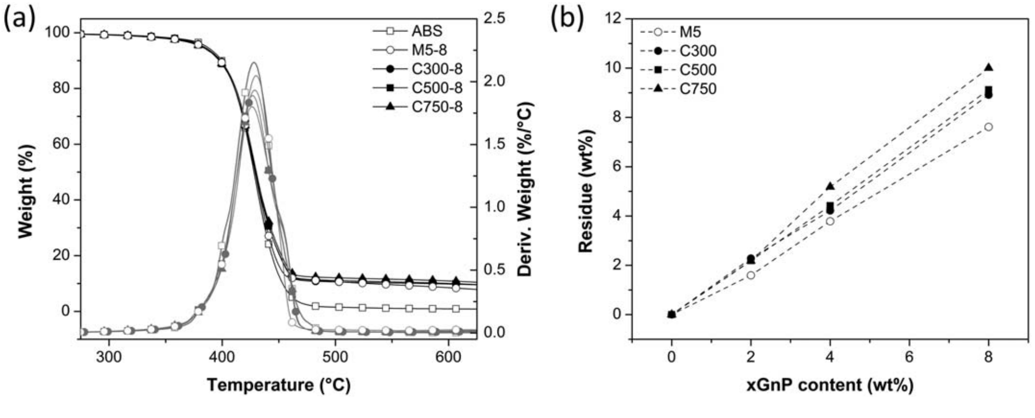

FIG. 4. Selected TGA curves of neat and nanofilled ABS–graphene performed under nitrogen atmosphere: (a) mass loss (black line), derivative of mass loss (gray line), and (b) relative residue at 600°C.

TABLE 2. Results of TGA analysis of neat and nanofilled ABS–graphene performed under nitrogen atmosphere.

Samples	$T_{d,max}$ (°C)	Mass loss (wt%)	MMLR (%/°C)	Residue at 600°C (wt%)	Residue at 800°C (wt%)
ABS	429.2	47.5	2.15	0.9	0.0
M5-2	428.3	48.5	2.13	2.5	0.9
M5-4	430.5	47.3	2.10	4.7	2.0
M5–8	430.0	48.2	2.05	8.5	3.9
C300-2	428.0	50.4	2.12	3.2	1.1
C300-4	429.2	50.2	2.04	5.1	2.9
C300-8	428.6	52.9	1.93	9.8	6.6
C500-2	428.1	50.2	2.14	3.1	0.7
C500-4	426.9	51.6	2.07	5.3	1.9
C500-8	426.9	54.3	1.89	10.0	5.8
C750-2	426.0	51.2	2.15	3.1	0.2
C750-4	427.1	54.4	2.05	6.1	2.2
C750-8	426.3	56.1	1.80	10.9	6.1

$T_{d,max}$, maximum degradation rate temperature; MMLR, maximum mass loss rate.

Moreover, the relative crystallinity (RC) of mold lubricant in ABS composites could be evaluated according to *Eq. 2*

$$\mathrm{RC}=100\times\frac{\Delta H_N}{3.6} \quad (2)$$

from the ratio of the normalized melting heat ΔH_N of the composite and the melting heat of pristine ABS pellets 3.6 J/g. It is interesting to observe that the percentage of crystallized mold lubricant was found to progressively decrease with the addition of filler, reaching about 36–39% in the case of C500-8 and C750-8, confirming a hindering effect of the graphene surface on the crystallizability of the mold lubricant, both in the first and especially in the second DSC scan (see Table 3).

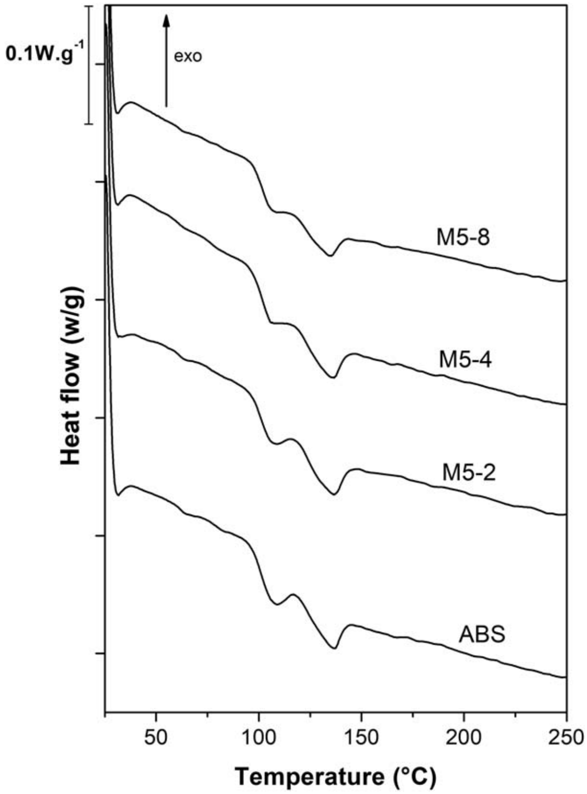

FIG. 5. Representative DSC thermograms (first heating scan) of neat ABS and nanocomposites at different content of xGnP-M5.

These findings not only suggest an interaction between the mold lubricant and the surface area of graphene, but also indirectly indicate a good dispersion of the filler.

Electromagnetic Interference Shielding Effectiveness (EMI SE)

The attenuation of the propagating electromagnetic wave in a conductive composite can be defined as electromagnetic interference shielding effectiveness (EMI SE), and it can be determined by the ratio of the incident power (P_{inc}) and the transmitted power (P_{trans}) according to *Eq. 3* [52]:

$$\mathrm{SE(dB)}=10\log\frac{P_{inc}}{P_{trans}} \quad (3)$$

Figure 7a–d shows the representative plots of EMI SE expressed in decibel (dB) of the neat ABS and various xGnP-filled nanocomposites in the frequency range from 8 to 12.4 GHz. An average EMI SE value of −0.74 dB for neat ABS was measured, indicating that the polymer is almost transparent to magnetic waves. As expected, the increase in the conductive filler content result in an improvement of EMI SE, as observed in literature for various carbon-based ABS composites [26, 53–55].

Nanocomposites containing C300, C500, and C750 exhibited similar electromagnetic attenuation, at the same xGnP content, almost independently on the surface area of the filler, in tentative relationship with the similar lateral dimension of 1–2 micron and similar thickness lower than 2 nm. However, nanocomposites filled with M5 nanofiller (thickness of 6 nm), showed a higher EMI SE, analogously to ABS composites filled with high structure

TABLE 3. Glass transition temperatures (T_g) of styrene–acrylonitrile phase, melting temperature (T_m), melting heat (ΔH_m), and relative crystallinity index (RC) of mold lubricant for ABS and relative nanocomposite as measured in DSC analysis.

	First heating				Second heating			
Samples	T_g (°C)	T_m (°C)	ΔH_m (J/g)	RC (%)	T_g (°C)	T_m (°C)	ΔH_m (J/g)	RC (%)
Pellets	101.3	138.9	3.6	100	104.3	138.7	3.0	83
ABS	100.7	136.4	3.1	86	103.3	137.1	2.8	78
M5-2	101.2	136.4	3.1	88	103.8	136.8	2.7	77
M5-4	102.0	134.9	2.9	84	103.3	135.7	2.5	72
M5–8	102.0	134.1	2.4	72	104.3	135.1	1.8	54
C300-2	102.0	135.4	2.6	74	104.3	138.6	2.0	57
C300-4	102.5	133.6	2.7	78	104.3	136.6	1.7	49
C300-8	102.3	132.3	2.2	66	105.1	134.8	1.1	33
C500-2	102.3	135.1	2.7	77	105.3	137.6	2.1	60
C500-4	102.0	132.4	2.6	75	104.8	135.5	1.7	49
C500-8	102.8	129.1	1.2	36	105.6	132.0	0.8	24
C750-2	102.0	134.9	2.7	77	105.2	137.3	2.1	60
C750-4	102.1	133.4	2.4	69	105.1	134.4	1.5	43
C750-8	103.0	128.9	1.3	39	105.5	129.5	0.7	21

carbon black [53]. Furthermore, the EMI SE of nanocomposites containing up to 4 wt% of xGnP is almost independent from the frequency, whereas nanocomposites with 8 wt% of xGnP showed a slight dependence of the shielding effectiveness on the frequency in the X-band.

The maximum of shielding effectiveness in ABS composites was obtained with the highest loading of xGnP (i.e., 8 wt%). In particular, EMI SE increased 257% after addition of GNP-C (C300, C500, and C750) from −0.7 to −2.5 dB, and 786% with graphene type M5 (from −0.7 to −6.2 dB). However, these results on graphene/ABS composites appears to be lower than those of other carbon-based ABS composites reported in literature. For instance, Sachdev et al. obtained a shielding efficiency of −60 dB after addition of 15 wt% of graphite in the X-band [26], whereas by using 10 wt% of multiwalled carbon nanotubes (MWCNTs) Jyoti et al. achieved a shielding efficiency of −39 dB in the Ku-band, 12–18 GHz [54]. The EMI SE typically required for commercial application is about −22.0 dB, which corresponds to <1% of transmitted electromagnetic wave [55]. The results reported in this work indicate that by using up to 8 wt% of xGnP into the ABS matrix, it is not possible to attain the EMI SE levels required for commercial applications.

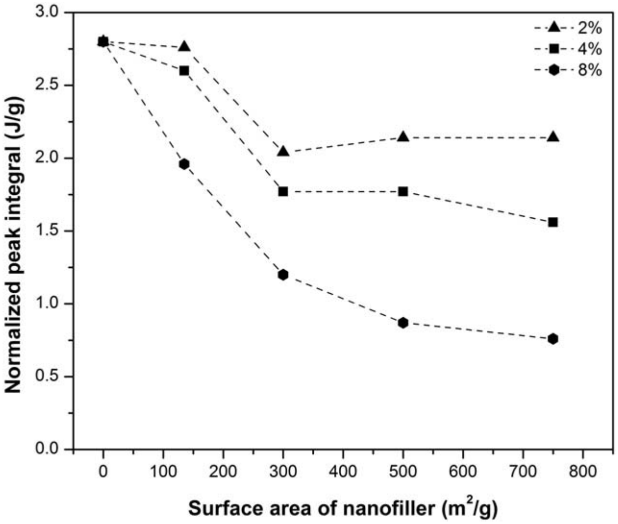

FIG. 6. Normalized melting heat (from second DSC heating) of mold lubricant as function of surface area and content of xGnP nanoplatelets in ABS nanocomposites.

The contribution of reflection (SE_R) and absorption (SE_A) to the total EMI SE of the composites was investigated. In the same time, the effect of multiple reflections (SE_M) was neglected, as commonly reported in literature [53, 56]. For this purpose, the complex scattering parameters that represent the reflection S_{11} (S_{22}) and transmission S_{12} (S_{21}) coefficients were compared with the incident electromagnetic wave, and were used to evaluate reflected power (P_{ref}), transmitted power (P_{trans}), and absorbed power (P_{abs}) according to the equations:

$$P_{ref}=\left|\frac{E_R}{E_I}\right|^2=|S_{11}|^2(=|S_{22}|^2) \tag{4}$$

$$P_{trans}=\left|\frac{E_T}{E_I}\right|^2=|S_{12}|^2(=|S_{21}|^2) \tag{5}$$

$$P_{abs}=1-(P_{ref}-P_{trans}) \tag{6}$$

Subsequently, the contribution of reflection SE_R and absorption SE_A to the total EMI SE was evaluated according to Eqs. 7–9.

$$SE_R(dB)=10\log\frac{P_{inc}}{P_{inc}-P_{ref}} \tag{7}$$

$$SE_A(dB)=10\log\frac{P_{inc}-P_{ref}}{P_{trans}} \tag{8}$$

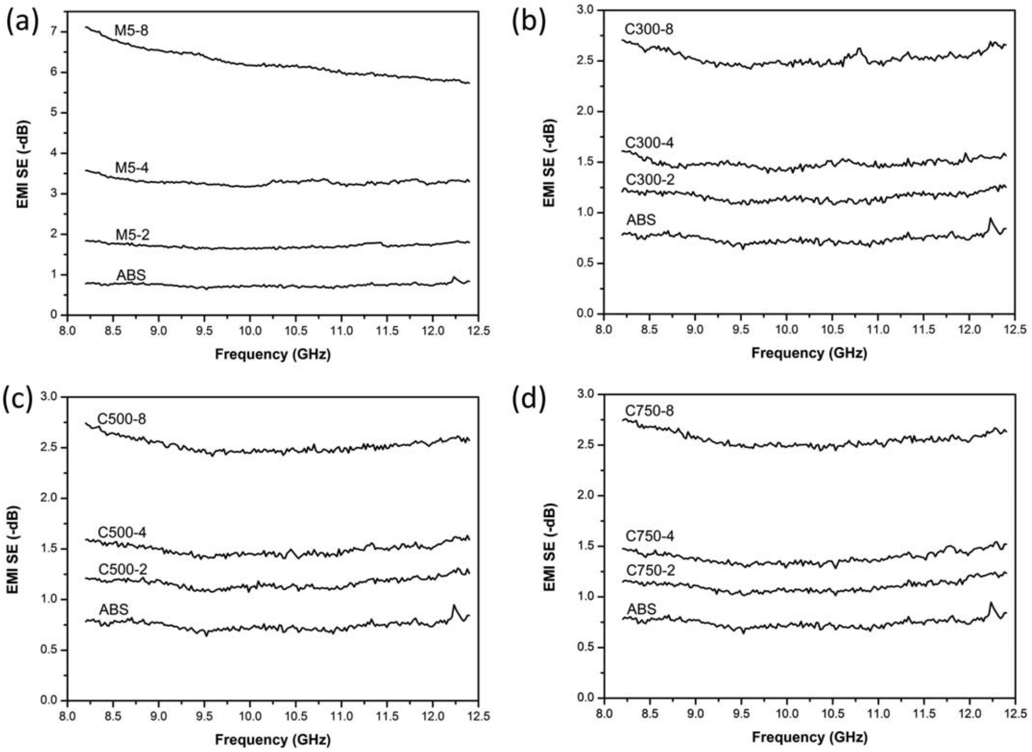

FIG. 7. EMI SE of nanocomposites containing different types of graphene nanoplatelets: (a) M5, (b) C300, (c) C500, and (d) C750. Standard deviation is lower than about 5% (0.04dB for ABS; 0.33dB for M5 nanocomposites; 0.07dB for Series C nanocomposites).

$$\begin{aligned}\mathrm{SE_{total}}(\mathrm{dB})=\mathrm{SE_A}+\mathrm{SE_R}=10\log\frac{P_{\mathrm{inc}}-P_{\mathrm{ref}}}{P_{\mathrm{trans}}}\\+10\log\frac{P_{\mathrm{inc}}}{P_{\mathrm{inc}}-P_{\mathrm{ref}}}=10\log\frac{P_{\mathrm{inc}}}{P_{\mathrm{trans}}}\end{aligned} \tag{9}$$

Due to the almost independence on frequency, the average values of reflection and absorption contributes in the range frequency of 8.2–12.4 GHz were reported and compared in Figure 8 as a function of graphene content.

For all compositions, the shielding by either reflection or absorption of composites increases with increasing xGnP content, resulting in higher EMI SE.

In particular, for all graphene/ABS composites the dominant shielding mechanism is the reflection, due to the platelet-shaped xGnP that provide higher surface area for interaction with the electromagnetic wave, as previously observed in carbon-based poly(styrene-b-ethylene-ran-butylene-b-styrene) (SEBS) composites [52]. However, it should be noted that other researchers reported that for different nanocomposites the shielding absorption contribute is higher than that of reflection one, $\mathrm{SE_A} > \mathrm{SE_R}$ [26, 53, 57, 58].

It is interesting to compare the results of graphene and graphene oxide nanoplatelets that have been recently used to improve the EMI SE of amorphous thermoplastic polymers. Yan et al. [57] achieved an ultra-efficient EMI shielding of −45.1 dB in the X-band, with 7 wt% of reduced graphene oxide, following a peculiar processing technique of segregation at high pressure starting from micrometric polystyrene powder. Following traditional processing conditions, King et al. prepared various composition of polycarbonate (PC) nanocomposites with GnP type M nanoparticles through twin screw compounding [59]. They reported no effect after addition 4 wt% of xGnP-M5, but only 15 wt% PC nanocomposite showed SE value of −6.3 dB at 0.8 GHz. Similarly, in the present research a lower percentage of xGnP-M5, 8 wt%, was shown to obtain −7.1 dB at 8.2 GHz in ABS nanocomposites produced by direct melt compounding. Following these results, it is possible to conclude that M5 nanoparticles appear more effective in EMI SE than C-type graphene nanoplatelets in ABS nanocomposites.

The better performance of ABS nanocomposites containing M5 can also be related to the higher average lateral dimensions of graphene (about 5 micron) with respect to C-type graphene nanoplatelets, and determining an increase in interaction with the radiation, and consequently an improvement of EMI SE.

In order to shed more light on EMI SE behavior, being related to low resistivity of single graphene nanoparticle, about 50×10^{-6} Ω cm and 1 Ω cm in parallel and in perpendicular direction respectively [60], the electrical resistivity of ABS and xGnP nanocomposites at highest graphene content (8 wt% i.e., about 4 vol%), has been compared and reported in Table 4. Volume resistivity of ABS (2.15×10^{15} Ω cm) was only slightly reduced after

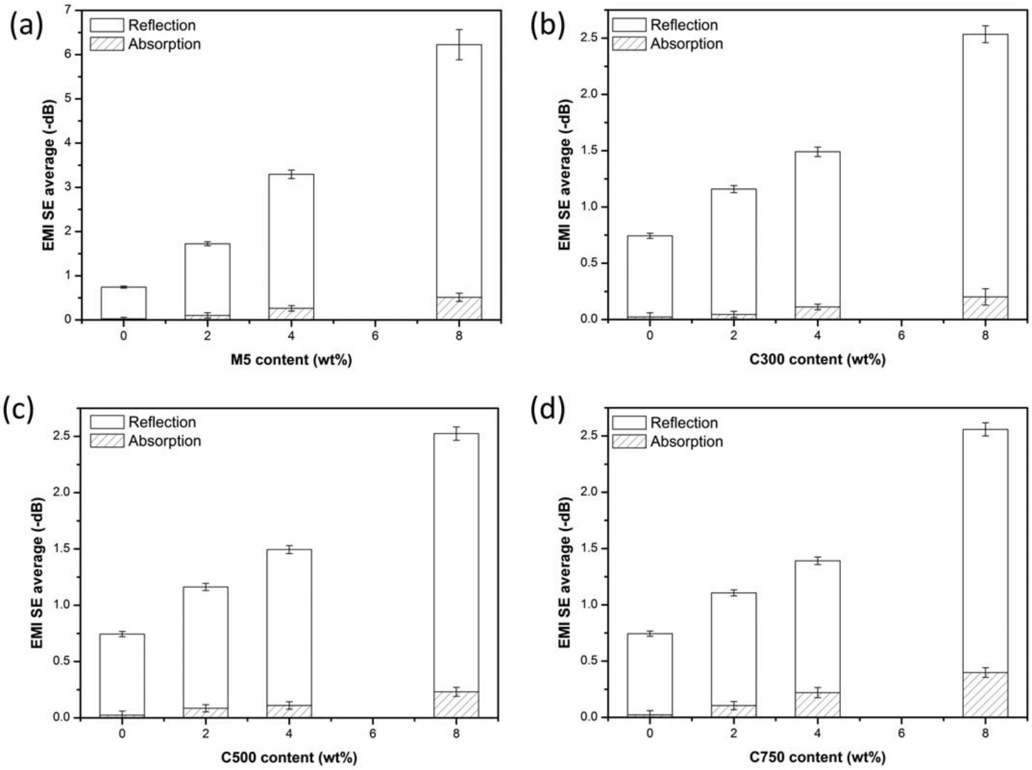

FIG. 8. Influence of absorption and reflection mechanisms on the EMI SE of nanocomposites containing different graphene nanoplatelets: (a) M5, (b) C300, (c) C500, and (d) C750, with various fillers contents. Standard deviation is in the range of 0.05–0.09 dB for absorption, and 0.2–0.5 dB for reflection, respectively.

addition of xGnP of Series C (about 0.9 × 10^{15} Ω cm), whereas a better improvement was obtained in composite containing M5 (1.8 × 10^{14} Ω cm). The higher the content of conductive filler, the higher the resistivity reduction, the higher the increase in EMI SE. The relationship between the decrease in resistivity and the effect of magnetic shield is shown in Figure 9 that correlates the better performance of M5 with reduced resistivity and the correspondent higher EMI SE. The relative volume resistivity however is not reduced enough to reach a conductive zone. Therefore, due to the low values of EMI SE achieved by using up to 8 wt% of xGnP, higher fractions of xGnP need to be incorporated in order to reach higher values, as reported by Merlini et al. [55], wherein SE levels required for commercial applications were obtained only after addition of 15 wt% of xGnP into a PU matrix.

It should be noted that King et al. after addition of xGnP-M5 at 8 wt% (5 vol%) in polycarbonate matrix reached a percolation threshold with electrical resistivity of 4.0 × 10^7 Ω cm [61].

Following these results, M5 nanoparticles appear the more promising xGnP candidate for the production ABS

TABLE 4. Volume resistivity and average EMI SE of ABS and nanocomposites with 8% wt of xGnP.

Samples	xGnP surface (m^2/g)	Electrical resistivity × 10^{-14} (Ω cm)[a]	EMI SE (−dB)[b]
ABS	—	21.5 ± 3.3	0.74 ± 0.04
C750-8	750	9.71 ± 2.57	2.53 ± 0.67
C500-8	500	8.03 ± 1.64	2.52 ± 0.66
C300-8	300	8.95 ± 3.12	2.56 ± 0.69
M5–8	120–150	1.75 ± 0.28	6.23 ± 0.33

[a] Average of three samples.

[b] Average between 8.2 and 12.4 GHz.

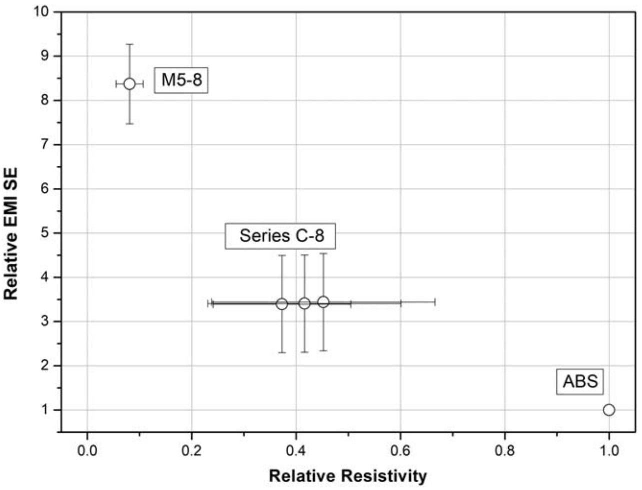

FIG. 9. Relative electromagnetic shield vs. relative resistivity of xGnP-ABS composite at 8 wt% of M5 and Series C.

TABLE 5. Tensile properties of nanocomposites as function of different xGnP type and content. Average values and standard deviation of at least five specimens are reported.

Samples	V_{f} (vol%)	E (GPa)	σ_{y} (MPa)	ε_{y} (%)	σ_{b} (MPa)	ε_{b} (%)	E_{norm}[a]
ABS	0	2,147 ± 118	39.0 ± 0.5	4.1 ± 0.2	29.9 ± 0.4	28.4 ± 5.2	nd[b]
M5-2	1.02	2,582 ± 86	36.4 ± 1.0	3.5 ± 0.1	29.1 ± 0.8	9.6 ± 2.8	10.1
M5-4	2.06	2,868 ± 202	35.7 ± 0.7	3.2 ± 0.1	31.5 ± 2.6	5.1 ± 1.5	8.4
M5–8	4.21	3,531 ± 282	35.4 ± 1.0	2.7 ± 0.1	33.3 ± 4.3	2.8 ± 0.2	8.1
C300-2	0.90	2,196 ± 74	38.6 ± 1.0	3.8 ± 0.2	29.3 ± 0.7	11.7 ± 6.0	1.1
C300-4	1.83	2,340 ± 101	39.8 ± 0.3	3.6 ± 0.1	33.8 ± 2.8	5.1 ± 1.2	2.3
C300-8	3.74	2,523 ± 224	37.8 ± 0.9	3.3 ± 0.2	37.2 ± 0.8	3.4 ± 0.3	2.2
C500-2	0.91	2,368 ± 184	41.4 ± 0.7	4.0 ± 0.2	33.2 ± 1.9	6.8 ± 2.5	5.2
C500-4	1.85	2,434 ± 179	40.7 ± 0.6	3.7 ± 0.2	38.9 ± 1.5	3.9 ± 0.3	3.3
C500-8	3.78	2,623 ± 101	39.3 ± 2.0	3.5 ± 0.1	38.8 ± 2.2	3.6 ± 0.3	2.8
C750-2	0.95	2,312 ± 348	41.0 ± 0.9	4.0 ± 0.2	33.1 ± 2.8	12.0 ±5.3	3.8
C750-4	1.93	2,271 ± 122	39.8 ± 0.7	3.6 ± 0.1	36.4 ± 1.6	4.0 ± 0.2	1.4
C750-8	3.94	2,527 ± 177	40.4 ± 2.5	3.4 ± 0.2	40.3 ± 2.4	3.4 ± 0.2	2.2

[a] Normalized value of the improvement of the modulus following Eq. *10*.

[b] Not defined.

nanocomposites in EMI SE applications; a minimum filler content of at least 12 wt% could be suggested.

Quasi-Static Tensile Tests

The tensile properties of nanocomposites with the different types of graphene are summarized in Table 5. It can be noticed that the elastic modulus of ABS increased proportionally to the filler loading. The modulus of composites containing the highest amount (8 wt%) of grade C xGnPs is increased from 2,147 MPa to 2,523 MPa (i.e., 17%), to 2,623 MPa (i.e., 22%), and to 2,527 MPa (i.e., 17%) for C300, C500, and C750 nanofillers, respectively. More effectively, the addition of M5 determined a higher increase in modulus for all the compositions, reaching 3,531 MPa (i.e., 64%) in nanocomposite containing 8 wt% of nanofiller. These better performances of M5 in increasing ABS stiffness appeared in agreement with literature data. For instance, King et al. reported an increase in tensile modulus of thermosetting epoxy of about 14% and 23% after addition of 6 wt% of xGnP-C300 and xGnP-M5, respectively [62]. An analogous and more evident effect was also reported by Wang et al. for epoxy nanocomposites containing 5% of graphene; they showed an increase in tensile modulus of about 22% after addition of C750, and an increase in 48% after addition of M5. Following their results and other literature data, Wang et al. attributed the superior behavior of xGnP-M5 nanoplatelets to the higher aspect ratio [10].

Moreover, the yield stress of ABS nanocomposite is fairly constant at about 39–41 MPa even after the addition of grade C xGnPs (C300, C750, and C500), whereas the effect of M5 nanofiller is to slightly reduce the yield strength (by about 9%). Concerning ultimate properties, the strain at break is markedly decreased up to 3–4% after addition of 8% of xGnP; correspondingly the stress at break reached a maximum of 37–40 MPa in nanocomposites containing graphene of C series, whereas only 33 MPa were reached in the case of M5 nanoplatelets.

The lower yield stress and strength of composites filled with M5 nanoparticles can be attributed to the poor adhesion between the ABS matrix and the nanofiller. Similarly, a significant reduction of strength in M5/epoxy nanocomposites [10, 62], and an almost constant strength in C750/epoxy nanocomposites with respect to pure matrix was also reported [10]. Wang et al. [10] attributed the higher strength and the better adhesion of C750 to the higher content of oxygen functional groups, in comparison to the lower adhesion and the lower oxygen content of M5.

However, to understanding the ultimate mechanical properties reported in Table 5, the simple explanation referred to the absolute content of oxygen is not exhaustive/satisfactory. Following a deeper interpretation of XPS analysis (Table 1, and Fig. 2b and c), the lower ultimate properties of xGnP-M5/nanocomposite and the reduced adhesion between matrix and filler, could be attributed not only to the lower content of ether/alcohol groups, but also to the significant content of sulfur and carbonyl groups on the surface of xGnP-M5. In general, the higher the content of ether/alcohol groups on graphene surface, the higher the adhesion to ABS matrix, and the higher the yield stress and strength.

The effect of xGnP-M5 on mechanical properties with respect to the Series C graphene nanoplatelets appeared similar for both thermosetting [10, 62] and thermoplastic matrices.

To compare the mechanical properties of ABS composites reported in literature, a normalized modulus was evaluated as follows:

$$\text{Normalized modulus} = E_{\mathrm{norm}} = \frac{E_{\mathrm{c}} - E_{\mathrm{i}}}{E_{\mathrm{i}} w_{\mathrm{f}}} \qquad (10)$$

where E_{c} is the modulus of ABS composite; E_{i} is the modulus of neat ABS, and w_{f} is the weight fraction of incorporated filler, as proposed by Pandey et al. [24].

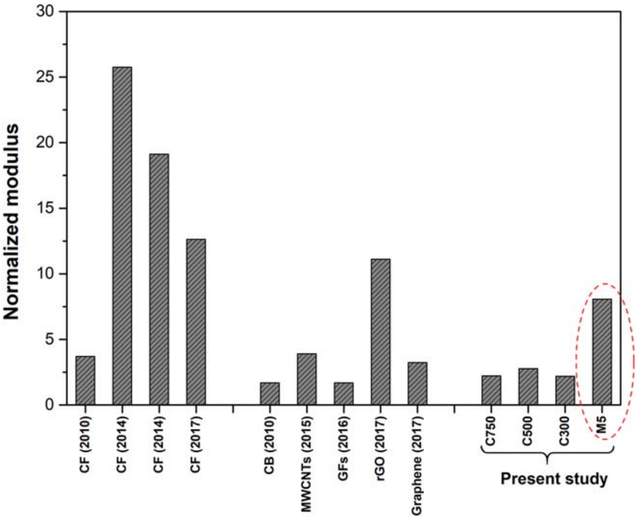

FIG. 10. Normalized modulus of ABS composites according *Eq. 10* after incorporation of different carbonaceous fillers, such as carbon black (CB [68]), MWCNTs [53], graphite flakes (GFs) [24], reduced graphene oxide (rGO [67]), graphene [69], and the xGnP nanoplatelets M5, C300, C500, and C750 of the present study. Carbon fiber (CF) composites produced by injection molding [66], compression molding [63], and additive manufacturing [64, 65] are also compared.

E_{norm} formally represents the percentage of modulus variation after addition of 1% of filler.

Figure 10 compares the normalized modulus at the highest weight fraction from *Eq. 10* of various carbon-based ABS nanocomposites produced from different processes. High normalized modulus values between 12 and 27 were calculated for carbon fiber (CF) composite produced by compression molding [63], or additive manufacturing [64, 65]; and lower values of 3.7 for short CF composite obtained by injection molding [66]. It is also worth noting the case of reduced graphene oxide (rGO) for which a normalized modulus of 11 was obtained, and attributed to the superior dispersion in ABS after chemical modification with respect to the scarce behavior of graphene oxide [67]. Different the situation of other lower size carbon fillers at micro or nano level, evaluated from recent literature data for ABS composites, for which the normalized modulus was determined in the range of 1.5–4.0, i.e. 1.7 after addition of 40 wt% of carbon black (CB) [68], 1.68 with 9 vol% of graphite flakes (GFs) [24], 3.9 with 10 wt% of MWCNTs [54], 3.2 with 7.5 wt% of graphene [69].

The addition of xGnP presented in this study, determined a normalized modulus in the range of 2.2–2.8 for C300, C500, and C750, and a remarkable value of 8.1 for M5 was reached at the highest filler content of 8 wt%. These results are comparable to those of other nanocomposites with xGnP dispersed in different matrices. For instance, in epoxy resin values of 2.3 and 3.9 were calculated for C300 and M5 according to the data provided by King et al. [62]; and higher normalized modulus could be obtained from the results of Wang et al. [10], i.e. 4.4 for C750 and 9.6 for M5. Moreover, in the case polycarbonate matrix, normalized modulus values of 3.6, 4.0, and 11.2 could be determined for carbon black, carbon nanotube, and graphene type M5, respectively [61].

It is possible to conclude that between the various examined graphenes, xGnP M5 exhibits the higher normalized modulus.

Modeling of Tensile Modulus

The empirical Halpin–Tsai model is a simple approach to predict the modulus of composite materials which takes into account the modulus of matrix E_{M} and filler E_{F}, filler aspect ratio ξ, volume fraction of filler V_{f}, assuming a homogeneous dispersion and perfect interfacial adhesion between polymer/filler [11, 62, 70–72]. The tensile modulus in both longitudinal E_{L} and transverse E_{T} directions can be predicted according to Halpin–Tsai model [73, 74] by the following equations:

$$E_{\mathrm{L}}=\frac{1+\xi\eta_{\mathrm{L}}V_{\mathrm{f}}}{1-\eta_{\mathrm{L}}V_{\mathrm{f}}}E_{\mathrm{M}} \tag{11}$$

$$E_{\mathrm{T}}=\frac{1+2\eta_{\mathrm{T}}V_{\mathrm{f}}}{1-n_{\mathrm{T}}V_{\mathrm{f}}}E_{\mathrm{M}} \tag{12}$$

where the parameters η_{L}, η_{T}, and ξ are defined in Eqs. 13–15:

$$\eta_{\mathrm{L}}=\frac{(E_{\mathrm{f}}/E_{\mathrm{M}})-1}{(E_{\mathrm{f}}/E_{\mathrm{M}})+\xi} \tag{13}$$

$$\eta_{\mathrm{T}}=\frac{(E_{\mathrm{f}}/E_{\mathrm{M}})-1}{(E_{\mathrm{f}}/E_{\mathrm{M}})+2} \tag{14}$$

$$\xi=\frac{2}{3}\frac{D_{\mathrm{f}}}{t_{\mathrm{f}}} \tag{15}$$

D_{f} and t_{f} represent diameter and thickness of graphene nanoplatelets, respectively.

The volume fraction V_{f} is linked to the weight fraction w_{f} through *Eq. 16*:

$$V_{\mathrm{f}}=\frac{w_{\mathrm{f}}\rho_{\mathrm{M}}}{w_{\mathrm{f}}\rho_{\mathrm{M}}+(1-w_{\mathrm{f}})\rho_{\mathrm{f}}} \tag{16}$$

where ρ_{M} and ρ_{f} are the density values of ABS matrix and graphene nanoplatelets, respectively.

Subsequently, the modulus of a composite with platelets filler long axis parallel to the loading direction (E^{Parallel}) and randomly oriented platelets fillers in all three-dimensional 3D-directions (E^{Random}) can be predicted according to literature [21, 75, 76] as follow:

$$E_{\mathrm{c}}^{\mathrm{Parallel}}=E_{\mathrm{L}} \tag{17}$$

$$E_{\mathrm{c}}^{\mathrm{Random}}=0.49E_{\mathrm{L}}+0.51E_{\mathrm{T}} \tag{18}$$

In the Halpin–Tsai model an experimental modulus for neat ABS of 2,147 MPa was considered (Table 5). The

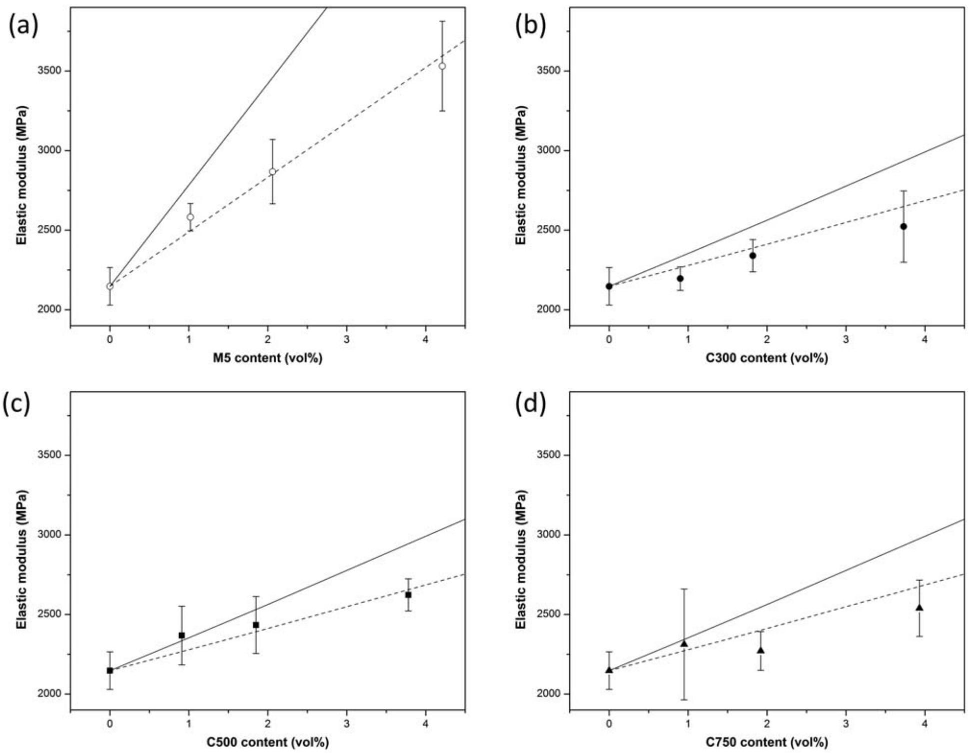

FIG. 11. Elastic modulus of nanocomposites with different type of graphene, i.e.: (a) M5 (○), (b) C300 (•), (c) C500 (■), and (d) C750 (▲). Prediction according Halpin–Tsai model with parallel and random orientation (according *Eqs. 17* and *18*) is shown by continuous and dot lines, respectively. Average values and standard deviation are reported in Table 5.

aspect ratios are considered equal to 19 for xGnP-C (C300, C500, and C750) as reported by Chong et al. [21] and 833 for xGnP-M5 ($D_f = 5{,}000$ nm and $t_f = 6$ nm). The outcome of the model largely depends on the value of tensile modulus of the xGnP (E_f). The "in the plane" tensile modulus of a single-layer graphene is reported to be as high as 1,000 GPa [21, 32, 77]. In prior works, a modulus of 250 GPa was considered for graphene by Gómez-Navarro et al. [78] and Mayoral et al. [79], while Mehdi et al. [80], and Pedrazzoli and Pegoretti [81] adopted a value of 70 GPa. Since xGnP consists of several layers of graphitic planes bonded by van der Waals dispersive forces, King et al. [62] proposed an elastic modulus of 36.5 GPa. In this study, an elastic modulus of 70 GPa has been tentatively assumed.

The comparison of experimental data with the two analytical models is depicted in Figure 11.

It is evident that the experimental modulus of nanocomposites containing xGnPs M5, C300, C500, and C750 is adequately well fitted by Halpin–Tsai model assuming a three-dimensional (3D) random orientation of all the fillers. These results are in conformity with the processing conditions (compounding and compression molding), where hardly any orientation is expected.

Fractography

Relative good dispersion of graphene in ABS matrix can be observed for all the compositions, as documented in Figure 12a1–d1 from the fracture surface of nanocomposites at xGnP loading of 8 wt%. For C300, C500, C750, and M5 nanocomposites, graphene nanoplatelets are likely to possess an almost random-like orientation as better shown in Figure 12a2–d2, which confirm the hypothesis of 3D randomly oriented nanoplatelets assumed in the Halpin–Tsai model. For M5 nanocomposites, largest graphene flakes can be visualized in Figure 12a2 and a3, composed of single and multilayer platelets, whose thickness appeared to be about 35–40 nm. It is worthwhile to observe that the fracture surface evidences a quite poor filler/matrix adhesion and wrinkles of graphene flakes can be also observed. These features could justify the lower yield stress of M5 nanocomposite (36 MPa) with respect to that of ABS (39MPa). However, the higher yield stress of C500 and C750 (40–41 MPa) could be associated with the lower size of the particles and to a better adhesion between ABS matrix and the xGnP nanoplatelets at higher oxygen content on the surface.

At the highest magnification, the larger dimension of single graphene can be evaluated with lateral width of about 5.3 micron, 2.7 micron, 580 nm and 410 nm for M5 (Fig. 12a3), C300(Fig. 12b3), C500 (Fig. 12c3), and C750 (Fig. 12d3), respectively. In particular, for C750 samples the smallest size of nanoparticle is confirmed. Moreover, thickness of about 25–35 nm can be evidenced for all C-type nanoparticles. These experimental geometrical dimensions appeared only partially in conformity to

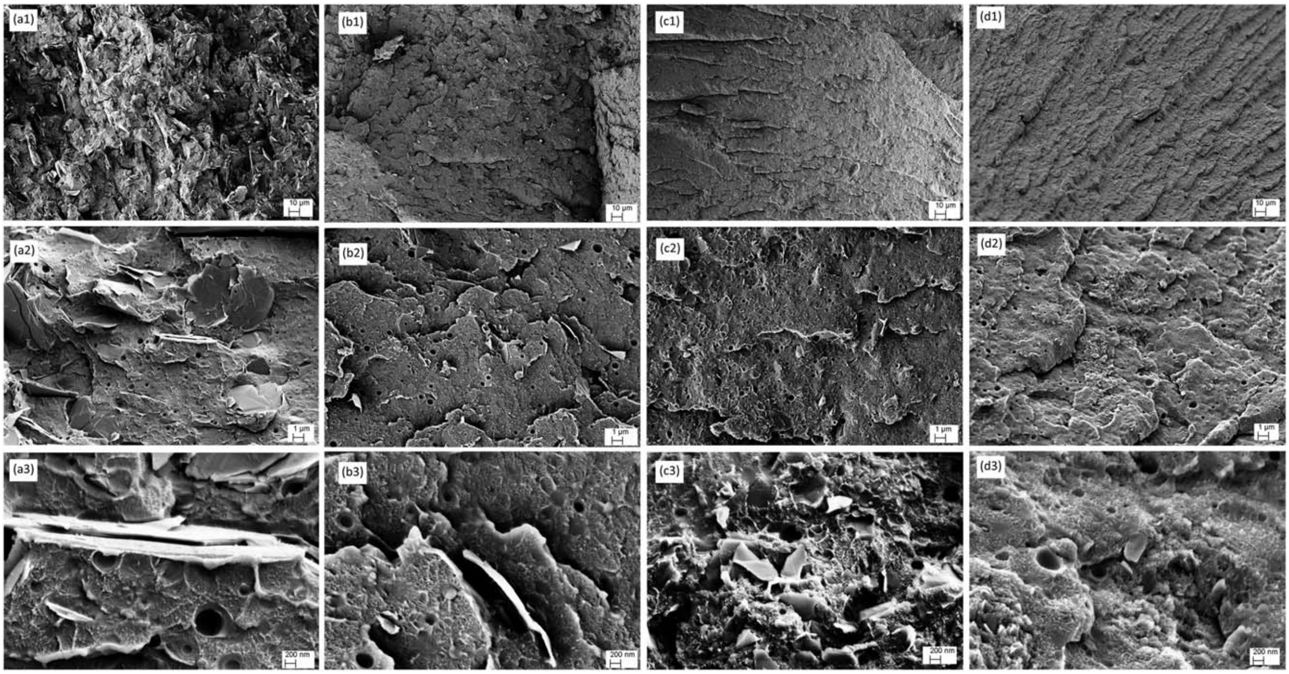

FIG. 12. (a) Representative SEM micrographs of M5 nanocomposite at graphene loading of 8 wt% at increasing magnification: 1,000× (a1), 10,000× (a2), and 50,000× (a3). (b) Representative SEM micrographs of C300 nanocomposite at graphene loading of 8 wt% at increasing magnification: 1,000× (b1), 10,000× (b2), and 50,000× (b3). (c) Representative SEM micrographs of C500 nanocomposite at graphene loading of 8 wt% at increasing magnification: 1,000× (c1), 10,000× (c2), and 50,000× (c3). (d) Representative SEM micrographs of C750 nanocomposite at graphene loading of 8 wt% at increasing magnification: 1,000× (d1), 10,000× (d2), and 50,000× (d3).

the producer data (Table 1). The larger thickness could be attributed to an overlapping effect of various tightly bonded nanoplatelets.

Some sub-micrometric cavities in the range of about 40–550 nm were also observed in all samples (see Fig. 12 at high magnification), which could be associated with the presence of mold lubricant additive. In fact during composite preparation, the mold lubricant could be not only partially dispersed into the matrix and/or on the filler surface, but it could be also separated in homogeneous spherical microparticles, that could be lost during the fracture formation. Moreover, the observed size of the nanofillers appeared proportional to the melting enthalpy of the mold lubricant, as shown in Table 3 and Figure 6.

CONCLUSIONS

The influence of various graphene nanoplatelets (xGnP-C300, C500, C700, and M5) on flow, thermal, electromagnetic shielding, electrical, and mechanical properties of ABS polymer was investigated. XPS analysis revealed an oxygen content of ether/alcohol groups for C300, C500, and C750 nanoparticles progressively increasing with the particle size reduction and the increase in surface area; in the case of M5 nanoplatelets the total oxygen content is also depending on the contribute of carbonyl groups and it is associated with traces of sulfur.

The melt flow of ABS almost linearly decreased by the presence of graphene up to 8 wt%. For C-type nanoparticles MFI values decreased proportionally to the filler surface area. Larger M5 nanoplatelets resulted to be the more promising in enhancing the shield efficiency to electromagnetic interference, while C300, C500, and C750 resulted in a moderate effect on ABS regardless of specific surface area. Correspondingly, M5 nanoplatelets determined a higher reduction of electrical resistivity with respect to the almost equivalent effect of C300, C500, and C750. However, it is necessary to point out that graphene content higher than 8% is required for practical applications in the field of electromagnetic shielding.

In addition, M5 nanoparticles showed the best reinforcement effect on the elastic modulus of composites in comparison of xGnP-C300, C500, and C750. Halpin–Tsai model was used to fit the tensile modulus of ABS/graphene composite. A 3D randomly oriented Halpin–Tsai model well fitted to the experimental modulus. Our results suggested that graphene nanoplatelets were 3D randomly oriented in ABS, in agreement with observation through scanning electron microscopy. Finally, it is worth to underline that, to the best of authors' knowledge, the improvement of normalized modulus observed for xGnP-M5/ABS composite is the highest ever reported in the open scientific literature on carbon-based fillers, except the case of carbon fiber and reduced graphene oxide ABS composites.

In conclusion, between the various xGnP nanoparticles studied in this research, M5 appears to be the most easy processing graphene filler in ABS composite, the most promising for resistivity reduction and for EMI applications, and the most effective in improving mechanical properties.

ACKNOWLEDGMENTS

Dul S. gratefully acknowledges AREAS+ EU Project of Erasmus Mundus Action 2 Programme for financial support.

REFERENCES

1. R.J. Crawford, *Plastics Engineering*, 3rd ed., Butterworth-Heinemann, Oxford, 1 (1998).
2. J.A. Brydson, *Plastics Materials (Seventh Edition)*, Butterworth-Heinemann, Oxford (1999).
3. E.A. Campo, *Industrial Polymers*, Carl Hanser Verlag GmbH & Co. KG, I, Munich (2007).
4. B. Ben Difallah, M. Kharrat, M. Dammak, and G. Monteil, *Mater. Des.*, **34**, 782 (2012).
5. F. Wang, Y. Zhang, B.B. Zhang, R.Y. Hong, M.R. Kumar, and C.R. Xie, *Compos. B: Eng.*, **83**, 66 (2015).
6. O. Ivanova, C. Williams, and T. Campbell, *Rapid Prototyping J.*, **19**, 353 (2013).
7. B.N. Turner, R. Strong, and S. A. Gold, *Rapid Prototyping J.*, **20**, 192 (2014).
8. F. Ning, W. Cong, J. Qiu, J. Wei, and S. Wang, *Compos. B: Eng.*, **80**, 369 (2015).
9. S. Dul, L. Fambri, and A. Pegoretti, *Compos. A: Appl. Sci. Manuf.*, **85**, 181 (2016).
10. F. Wang, L.T. Drzal, Y. Qin, and Z. Huang, *J. Mater. Sci.*, **50**, 1082 (2015).
11. A. Duguay, J. Nader, A. Kiziltas, D. Gardner, and H. Dagher, *Appl. Nanosci.*, **4**, 279 (2014).
12. M. Mehrali, E. Sadeghinezhad, S.T. Latibari, S.N. Kazi, M. Mehrali, M.N.B.M. Zubir, and H.S.C. Metselaar, *Nanoscale Res. Lett.*, **9**, 15 (2014).
13. B. Li and W.H. Zhong, *J. Mater. Sci.*, **46**, 5595 (2011).
14. X. Jiang and L.T. Drzal, *Polym. Compos.*, **31**, 1091 (2010).
15. K. Kalaitzidou, H. Fukushima, and L.T. Drzal, *Carbon*, **45**, 1446 (2007).
16. M. Mehrali, S.T. Latibari, M. Mehrali, T.M. Indra Mahlia, H.S. Cornelis Metselaar, M.S. Naghavi, E. Sadeghinezhad, and A.R. Akhiani, *Appl. Thermal Eng.*, **61**, 633 (2013).
17. M. Kim, S.-H. Hwang, B.-J. Kim, J.-B. Baek, H.S. Shin, H.W. Park, Y.-B. Park, I.-J. Bae, and S.-Y. Lee, *Compos. B: Eng.*, **66**, 511 (2014).
18. D. Pedrazzoli and A. Pegoretti, *Compos. A: Appl. Sci. Manuf.*, **66**, 25 (2014).
19. T.D. Thanh, L. Kaprálková, J. Hromádková, and I. Kelnar, *Eur. Polym. J.*, **50**, 39 (2014).
20. D.R. Klimek-McDonald, J.A. King, I. Miskioglu, E.J. Pineda, and G.M. Odegard, *Polym. Compos.*, (2016).
21. H.M. Chong, S.J. Hinder, and A.C. Taylor, *J. Mater. Sci.*, **51**, 8764 (2016).
22. S. Basu, M. Singhi, B.K. Satapathy, and M. Fahim, *Polym. Compos.*, **34**, 2082 (2013).
23. X. Pang, X. Shi, X. Kang, M. Duan, and M. Weng, *Polym. Compos.*, **37**, 2673 (2016).
24. A.K. Pandey, R. Kumar, V.S. Kachhavah, and K.K. Kar, *RSC Adv.*, **6**, 50559 (2016).
25. C. Heo, H.-G. Moon, C.S. Yoon, and J.-H. Chang, *J. Appl. Polym. Sci.*, **124**, 4663 (2012).
26. V.K. Sachdev, K. Patel, S. Bhattacharya, and R.P. Tandon, *J. Appl. Polym. Sci.*, **120**, 1100 (2011).
27. C. Gao, S. Zhang, F. Wang, B. Wen, C. Han, Y. Ding, and M. Yang, *ACS Appl. Mater. Interfaces*, **6**, 12252 (2014).
28. F.M. Uhl, Q. Yao, and C.A. Wilkie, *Polym. Adv. Technol.*, **16**, 533 (2005).
29. N. Hong, J. Zhan, X. Wang, A.A. Stec, T. Richard Hull, H. Ge, W. Xing, L. Song, and Y. Hu, *Compos. A: Appl. Sci. Manuf.*, **64**, 203 (2014).
30. H.S. Dahiya, N. Kishore, and R.M. Mehra, *J. Appl. Polym. Sci.*, **106**, 2101 (2007).
31. R.H. Pour, A. Hassan, M. Soheilmoghaddam, and H.C. Bidsorkhi, *Polym. Compos.*, **37**, 1633 (2016).
32. XG Sciences. xGnp® Graphene Nanoplatelets Grade M Product Data from http://xgsciences.com/products/graphene-nanoplatelets/grade-m/ consulted on October 18th (2017).
33. Versalis S.p.A SINKRAL® L 322- ABS Product Data from http://www.materialdatacenter.com/ms/en/Sinkral/Versalis+S%252Ep%252EA/SINKRAL%C2%AE+L+322/c09cddeb/1895 consulted on October 18th (2017).
34. S. Biniak, G. Szymański, J. Siedlewski, and A. Świątkowski, *Carbon*, **35**, 1799 (1997).
35. B. Quan, S.-H. Yu, D.Y. Chung, A. Jin, J.H. Park, Y.-E. Sung, and Y. Piao, *Sci. Rep.*, **4**, 5639 (2014).
36. A. Boldizar and K. Möller, *Polym. Degrad. Stab.*, **81**, 359 (2003).
37. P. Noorunnisa Khanam, M.A. AlMaadeed, M. Ouederni, E. Harkin-Jones, B. Mayoral, A. Hamilton, and D. Sun, *Vacuum*, **130**, 63 (2016).
38. H. Kim and C.W. Macosko, *Polymer*, **50**, 3797 (2009).
39. X. Wang, L. Song, H. Yang, H. Lu, and Y. Hu, *Ind. Eng. Chem. Res.*, **50**, 5376 (2011).
40. H. Oxfall, G. Ariu, T. Gkourmpis, R.W. Rychwalski, and M. Rigdahl, *Express Polym. Lett.*, **9**, 66 (2015).
41. J.R. Potts, D.R. Dreyer, C.W. Bielawski, and R.S. Ruoff, *Polymer*, **52**, 5 (2011).
42. E. Kuzdzal, B. Cichy, and S. Dulik, *CHEMIK*, **70**, 185 (2016).
43. X. Wei, D. Li, W. Jiang, Z. Gu, X. Wang, Z. Zhang, and Z. Sun, *Sci. Rep.*, **5**, 11181 (2015).
44. M.H. Al-Saleh, B.A. Al-Saidi, and R.M. Al-Zoubi, *Polymer*, **89**, 12 (2016).
45. M.E. Achaby, F.E. Arrakhiz, S. Vaudreuil, A.e.K. Qaiss, M. Bousmina, and O. Fassi-Fehri, *Polym. Compos.*, **33**, 733 (2012).
46. H. Blom, R. Yeh, R. Wojnarowski, and M. Ling, *J. Thermal Anal. Calorim.*, **83**, 113 (2006).
47. P. Singh and A.K. Ghosh, *Mater. Des.*, **55**, 137 (2014).
48. T.F. Reed, H.E. Bair, and R.G. Vadimsky, "The Causes of Pitting and Haze on Molded ABS Plastic Surfaces," in

Recent Advances in Polymer Blends, Grafts, and Blocks, L. H. Sperling, Ed., Springer US, Boston, MA, 359 (1974).

49. H.E. Bair, D.J. Boyle, and B. Twombly, *J. Thermal Anal.*, **46**, 955 (1996).
50. S. Dul, H. Mahmood, L. Fambri, and A. Pegoretti, “Graphene–ABS nanocomposites for fused deposition modelling,” in Proceedings of ECCM17 – 17th European Conference on Composite Materials, Munich, Germany (2016).
51. H.E. Bair, “Thermal Analysis of Additives in Polymers,” in *Thermal Analysis*, E. Turi Ed., Academic Press Inc, London (UK) (1981).
52. S. Kuester, C. Merlini, G.M.O. Barra, J.C. Ferreira, Jr A. Lucas, A.C. de Souza, and B.G. Soares, *Compos. B: Eng.*, **84**, 236 (2016).
53. M.H. Al-Saleh, W.H. Saadeh, and U. Sundararaj, *Carbon*, **60**, 146 (2013).
54. J. Jyoti, S. Basu, B.P. Singh, and S.R. Dhakate, *Compos. B: Eng.*, **83**, 58 (2015).
55. C. Merlini, A. Pegoretti, P.C. Vargas, T.F.d. Cunha, S.D.A.S. Ramôa, B.G. Soares, and G.M.O. Barra, *Polym. Compos* in press.
56. T.K. Gupta, B.P. Singh, S. Teotia, V. Katyal, S.R. Dhakate, and R.B. Mathur, *J. Polym. Res.*, **20**, 169 (2013).
57. D.-X. Yan, H. Pang, B. Li, R. Vajtai, L. Xu, P.-G. Ren, J.-H. Wang, and Z.-M. Li, *Adv. Funct. Mater.*, **25**, 559 (2015).
58. C. Merlini, G.M.O. Barra, M.D.P.P. da Cunha, S.D.A.S. Ramôa, B.G. Soares, and A. Pegoretti, *Polym. Compos.*, **38**, 2146 (2017).
59. J.A. King, W.A. Pisani, D.R. Klimek-McDonald, W.F. Perger, and G.M. Odegard, *J. Appl. Polym. Sci.*, **132**, 42719 (2015).
60. L.T. Drzal, http://xgsciences.com/wp-content/uploads/2013/04/Drzal-Presentation.pdf consulted on October 18th, 2017 (2013).
61. J.A. King, M.D. Via, F.A. Morrison, K.R. Wiese, E.A. Beach, M.J. Cieslinski, and G.R. Bogucki, *J. Compos. Mater.*, **46**, 1029 (2012).
62. J.A. King, D.R. Klimek, I. Miskioglu, and G.M. Odegard, *J. Compos. Mater.*, **49**, 659 (2015).
63. H.L. Tekinalp, V. Kunc, G.M. Velez-Garcia, C.E. Duty, L.J. Love, A.K. Naskar, C.A. Blue, and S. Ozcan, *Compos. Sci. Technol.*, **105**, 144 (2014).
64. D. Jiang and D.E. Smith, *Addit. Manuf.*, **18**, 84 (2017).
65. L.J. Love, V. Kunc, O. Rios, C.E. Duty, A.M. Elliott, B.K. Post, R.J. Smith, and C.A. Blue, *J. Mater. Res.*, **29**, 1893 (2014).
66. J. Li and Y.F. Zhang, *J. Reinforced Plast. Compos.*, **29**, 1727 (2010).
67. V. Panwar and K. Pal, *Compos. B: Eng.*, **114**, 46 (2017).
68. J.-W. Lee, J.-C. Lee, J. Pandey, S.-H. Ahn, and Y.J. Kang, *J. Compos. Mater.*, **44**, 1701 (2010).
69. S. Vikas, G. Meenakshi, and J. Prashant, *Indian J. Sci. Technol.*, **10**, 1 (2017).
70. J. Liang, Y. Huang, L. Zhang, Y. Wang, Y. Ma, T. Guo, and Y. Chen, *Adv. Funct. Mater.*, **19**, 2297 (2009).
71. J.C.H. Affdl and J.L. Kardos, *Polym. Eng. Sci.*, **16**, 344 (1976).
72. K. Kalaitzidou, H. Fukushima, and L.T. Drzal, *Compos. Sci. Technol.*, **67**, 2045 (2007).
73. J.C. Halpin, and T.W. Tsai, Effect of environmental factors on composite materials; Air Force Technical Report AFML-TR 67-423. Dayton, OH: Wright Aeronautical Laboratories; (1967).
74. J.C. Halpin, *J. Compos. Mater.*, **3**, 732 (1969).
75. M.A. Van Es, PhD Thesis, “Polymer-Clay Nanocomposites: The Importance of Particle Dimensions,” in *Faculty of Applied Sciences*. Delft University of Technology (2001).
76. T.D. Fornes and D.R. Paul, *Polymer*, **44**, 4993 (2003).
77. C. Lee, X. Wei, J.W. Kysar, and J. Hone, *Science*, **321**, 385 (2008).
78. C. Gómez-Navarro, M. Burghard, and K. Kern, *Nano Lett.*, **8**, 2045 (2008).
79. B. Mayoral, E. Harkin-Jones, P.N. Khanam, M.A. AlMaadeed, M. Ouederni, A.R. Hamilton, and D. Sun, *RSC Adv.*, **5**, 52395 (2015).
80. K. Mehdi, P. Raghuram V, B. Md A, and K. Kalaitzidou, *Carbon Lett.*, **11**, 325 (2010).
81. D. Pedrazzoli and A. Pegoretti, *J. Reinforced Plast. Compos.*, **33**, 1682 (2014).